Optimization design of a new hybrid magnetic circuit motor

MINGLING GAO[1]✉, SHILONG YAN[1], CHENGLONG YU[2], WENJING HU[1],
HUIHUI GENG[1], HONGBIN YIN[1], MINGJUN XU[1], YUFENG ZHANG[1]

[1]*Shandong University of Technology*
266 Xincun West Road, Zhangdian District, Zibo, Shandong Province, China
[2]*Zibo Yongtai Motor Co., Ltd*
Zichuan District, Zibo, Shandong, China

e-mail: {✉ gml_3437/zbytdj}@sina.com, {yanshilong97/hbinyin}@163.com,
{huwenjing/huihuigeng}@sdut.edu.cn, {20402010115/20601010005}@stumail.sdut.edu.cn

Abstract: The combination of permanent magnets and electrically excited windings creates an air gap magnetic field. The development of a hybrid magnetic circuit motor with an adjustable magnetic field is of great significance. This article introduces a hybrid magnetic circuit motor design that combines salient pole electromagnetic and permanent magnets. A tubular magnetic barrier has been designed to reduce inter-pole leakage and enhance the usage rate of permanent magnets in the hybrid magnetic circuit motor. The optimum eccentricity of the rotor has been accurately designed, resulting in an improved sinusoidal distribution of the air gap magnetic density waveform. An analysis of the static composite magnetic field under various excitation currents has been conducted, showcasing the capability of the hybrid magnetic circuit motor to stably adjust the air gap flux density level and output torque. A prototype has undergone comprehensive trial production and testing, conclusively confirming the machine's superior output performance.

Key words: combination of electromagnetic and permanent magnets, hybrid magnetic circuit, optimization of rotor structure

1. Introduction

The use of fossil fuels has created serious problems such as environmental pollution and resource depletion, leading to the establishment of strict environmental legislation and emission standards globally to reduce greenhouse gas emissions such as CO_2 and NO_x [1–4]. With the

introduction of China's dual carbon policy, the automotive industry has become a key area for the transformation to new energy [5, 6]. The motor is the core component of an electric vehicle, and it is essential to develop a motor that combines the advantages of high efficiency and high-power density of permanent magnet motors with the smooth and adjustable air gap magnetic field characteristics of electric excitation motors.

Yang C.X. proposed an axial-radial flux type permanent magnet synchronous motor [7]. The motor adds an axial excitation part to both sides and a conductive end cover to close the axial magnetic circuit. Paplicki P. proposed a new hybrid excited synchronous machine [8], in which the stator is placed on both sides and an excitation coil is placed between the two stators. The magnitude of the magnetic field can be adjusted by varying the current flowing into the excitation coil. Scholar Lin N. proposed a new type of hybrid excitation synchronous motor [9]. The full permanent magnet pole is located in the middle position, and the auxiliary part is located on both sides of the full permanent magnet pole. The permanent magnet surface is attached to the rotor core, and two sets of annular excitation coils are arranged inside the stator core to form an auxiliary excitation winding, forming a parallel magnetic circuit with the permanent magnet. Kwon B. proposed a new type of hybrid excitation wound synchronous motor [10]. This motor adds an auxiliary iron core and permanent magnet to the traditional wound synchronous motor. The permanent magnet is magnetized radially in the same direction as the magnetic field generated by electric excitation, forming a parallel hybrid excitation mode. Wardach M. proposed a hybrid excited machine with flux barriers and magnetic bridges [11]. The rotor is composed of an iron core with a U-shaped magnetic barrier, a flux bridge, and a permanent magnetic pole. The flux bridge is placed in the middle of the rotor to change the direction of magnetic flux distribution. Dr. Nakai proposed a new type of variable magnetic field circular wound permanent magnet motor [12]. The rotor of the motor is composed of a permanent magnet and a salient pole iron core, forming a clockwise pole structure. The axial end of the salient pole rotor iron core is wound with excitation windings on both sides, the motor has good magnetic regulation ability.

To shorten the axial length of the motor and improve the output efficiency of the motor, a new hybrid magnetic circuit motor structure is proposed. The magnetic circuit direction of the new structure is analyzed, and the parameters of the V-shaped permanent magnet and radial permanent magnet that make up the permanent magnet source are optimized. To further improve the performance of the hybrid magnetic circuit motor, the improvement effect of the tube-type magnetic barrier and the eccentricity of the rotor pole surface on the air gap magnetic density is analyzed in sequence. Conduct electromagnetic coupling simulation analysis on the optimized hybrid magnetic circuit drive motor, obtain the static synthesized magnetic field and output characteristics under different excitation currents, and make a prototype for testing.

2. Electromagnetic field analysis of hybrid magnetic circuit motor

Figure 1 displays a hybrid magnetic circuit motor comprised of a stator and a rotor with salient poles, integrating both salient electromagnetic and permanent magnetic poles. The salient pole rotor presents a T-shaped structure, with each pole of the iron core located in an excitation coil with an equal number of winding turns. The excitation coils between adjacent pole bodies have opposite winding directions. After energizing the excitation coil with direct current, it can generate

N and S poles that are spaced apart on the salient pole surface. The combined magnetic pole is placed at each pole shoe, consisting of a V-shaped permanent magnet, a radial permanent magnet, and a surface mounted permanent magnet. The V-shaped permanent magnet is embedded in the outer middle of each pole of the salient rotor, the radial permanent magnet is placed in the middle of the V-shaped permanent magnet, and the surface mounted permanent magnet is placed at the center of the outer circle of each pole shoe of the salient rotor and fixed with pole shoes. The polarity of each magnetic pole within the same salient pole is the same, and the polarity generated on the rotor surface between adjacent magnetic poles is arranged in intervals between N and S poles. Table 1 presents the parameters of the hybrid magnetic circuit motor. At this stage, a forward current is supplied to the excitation direct current coil.
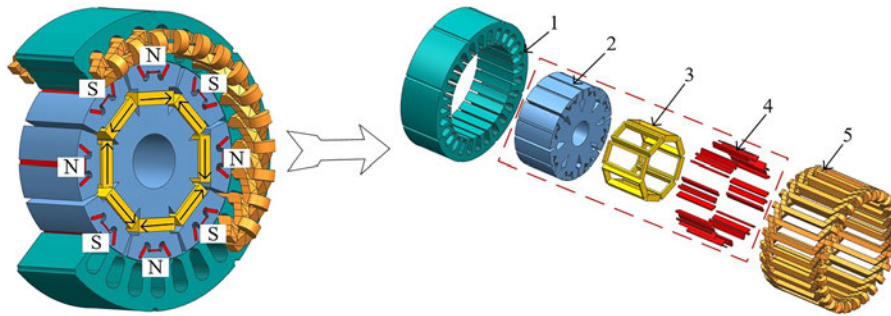
Fig. 1. Structure of the hybrid magnetic circuit motor: 1 -stator core; 2 – rotor core; 3 – excitation DC coil; 4 – permanent magnets; 5 – stator winding

Table 1. Performance parameters of hybrid magnetic circuit motor

Parameter name	Value	Unit	Parameter name	Value	Unit
Rated power	5	kW	Inner diameter of stator	107	mm
Rated torque	15.9	N·m	Outer diameter of stator	160	mm
Rated speed	3 000	r·min^{-1}	Axial length	80	mm

Figure 2 depicts the direction of the magnetic flux path in the hybrid magnetic circuit motor for different excitation states. In the absence of electric excitation, the combined magnetic pole generates a permanent magnetic flux path as shown in Fig. 2(a). The three magnetic flux paths provide magnetic flux independently, and there is no interference between the two. When current is applied to the excitation winding, an electric excitation magnetic flux path is generated in addition to permanent magnetic fluxes 1, 2, and 3. This can be observed in the stator and rotor as depicted in Fig. 2(b).

The calculation of the air gap magnetic field is the basis for analyzing the performance of the motor, and the subdomain method is applied to analyze the magnetic field changes of the salient permanent magnet part [13–15]. Divide the salient pole motor into four subdomains in sequence: stator slot subdomain 1, stator notch subdomain 2, air gap subdomain 3, and permanent magnet subdomain 4. Poisson's equation is applied in subdomain 1 and subdomain 4, and Laplace's equation is applied in subdomain 2 and subdomain 3 [16].
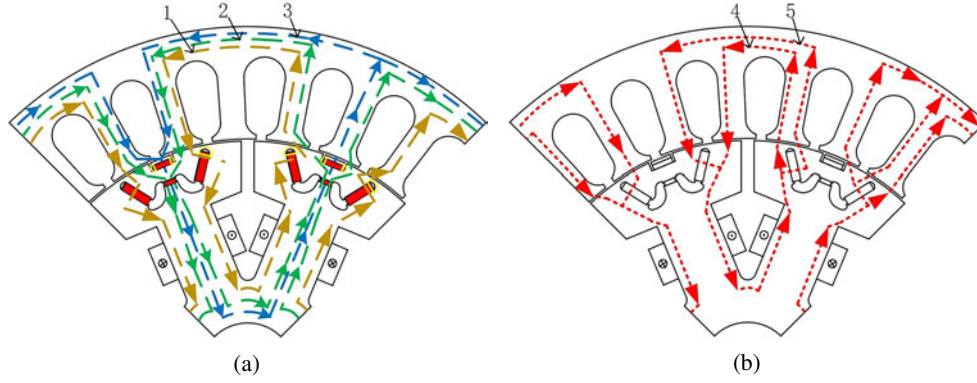
Fig. 2. Magnetic flux path direction diagram of hybrid magnetic circuit motor: (a) permanent magnet flux path; (b) electric excitation magnetic flux path

The stator slot subdomain magnetic density can be expressed as:

$$
\begin{aligned}
B_{1r} = {} & -E_{n_1} \sum_{n_1} \left\{ \left[A^1 \left(\frac{R_4}{R_5} \right) \left(\frac{r}{R_5} \right)^{n_1} + B^1 \left(\frac{r}{R_4} \right)^{n_1} \right] \right. \\
& - \frac{2\mu_0 \left(J_{i1} + J_{i2} \right) \sin\left(\frac{n_1 \pi}{2} \right)}{b_{\mathrm{sa}} r \left[\left(\frac{n\pi}{b_{\mathrm{sn}}} \right)^2 - 4 \right]} \left[r^2 - \frac{2}{E_{n_1}} R_5^2 \left(\frac{r}{R_4} \right)^{n_1} \right] \right\} \\
& \times \sin\left[\left(\frac{n_1 \pi}{b_{\mathrm{sn}}} \right) \left(\alpha_{\mathrm{t}} + b_{\mathrm{sn}} - \alpha_1 \right) \right],
\end{aligned} \tag{1}
$$

$$
\begin{aligned}
B_{1t} = {} & \frac{\mu_0}{2} - J_{i0} r \ln r + \frac{\mu_0}{4} J_{i0} r \\
& - \sum_{n_1} \left\{ n_1 \left[A^1 \left(\frac{R_4}{R_5} \right) \left(\frac{r}{R_5} \right)^{n_1 - 1} + B^1 \left(\frac{r}{R_4} \right)^{n_1 - 1} \right] \cos\left[E_{n_1} \left(\alpha_{\mathrm{t}} + b_{\mathrm{sn}} - \alpha_i \right) \right] \right. \\
& - \mu_0 \frac{2 \left(J_{i1} + J_{i2} \right) \sin\left(\frac{n_1 \pi}{2} \right)}{n_1 \pi \left[\left(\frac{n_1 \pi}{b_{\mathrm{sn}}} \right)^2 - 4 \right]} \left[2r - \frac{2}{E_{n_1}} n_1 R_5^2 \left(\frac{r}{R_4} \right)^{n_1 - 1} \right] \\
& \left. \cos\left[\left(\frac{n_1 \pi}{b_{\mathrm{sn}}} \right) \left(\alpha_t + b_{\mathrm{sn}} - \alpha_1 \right) \right] \right\},
\end{aligned} \tag{2}
$$

where: B_{1r} is the radial component of stator slot subdomain magnetic density, B_{1t} is the tangential component of stator slot subdomain magnetic density, n_1 is the logarithm of spatial harmonics in the stator slot subdomain, α_t is the circumferential angle, A^1 and B^1 are the harmonic coefficient of the stator slot subdomain, R_4 is the radius of the circle at the bottom of the stator slot, R_5 is the radius of the circle where the top of the stator slot is located.

The stator notch subdomain magnetic density can be expressed as:

$$B_{2r} = -\frac{n_2}{r} \sum_{n_2} \left\{ \left[A^2 \left(\frac{r}{R_4} \right)^{n_2} + B^2 \left(\frac{r}{R_3} \right)^{-n_2} \right] \sin\left[n_2 \left(\alpha + b_{\text{sk}} - \alpha_i \right) \right] \right.$$
$$\left. - \left[C^2 \left(\frac{r}{R_4} \right)^{n_2} - D^2 \left(\frac{r}{R_3} \right)^{-n_2} \right] \cos\left[n_2 \left(\alpha + b_{\text{sk}} - \alpha_i \right) \right] \right\}, \tag{3}$$

$$B_{2t} = -\sum_{n_2} \left\{ n_2 \left[A^2 \left(\frac{r}{R_4} \right)^{m-1} - B^2 \left(\frac{r}{R_3} \right)^{-n_2-1} \right] \cos\left[n_2 \left(\alpha + b_{\text{sk}} \alpha_i \right) \right] \right.$$
$$\left. - n_2 \left[C^2 \left(\frac{r}{R_4} \right)^{n_2-1} + D^2 \left(\frac{r}{R_3} \right)^{-n_2-1} \right] \sin\left[n_2 \left(\alpha + b_{\text{sk}} - \alpha_i \right) \right] \right\}, \tag{4}$$

where: B_{2r} is the radial component of stator notch subdomain magnetic density, B_{2t} is the tangential component of stator notch subdomain magnetic density, A^2, B^2, C^2 and D^2 are the harmonic coefficient of the stator slot subdomain, n_2 is the logarithm of spatial harmonics in the stator slot subdomain, R_3 is the inner radius of stator.

The radial and tangential components of the magnetic density in the air gap subdomain can be expressed as [17]:

$$B_{3r} = -\frac{n_3}{r} \sum_{n_3} \left[A^3 \left(\frac{r}{R_3} \right)^{n_3} + B^3 \left(\frac{r}{R_2} \right)^{-n_3} \right] \sin\left(n_3 \alpha \right)$$
$$+ \frac{n_3}{r} \sum_{n_3} \left[C^3 \left(\frac{r}{R_3} \right)^{n_3} + D^3 \left(\frac{r}{R_2} \right)^{-n_3} \right] \cos\left(n_3 \alpha \right), \tag{5}$$

$$B_{3t} = -\sum_{n_3} \left[n_3 A^3 \left(\frac{r}{R_3} \right)^{n_3-1} - n_3 B^3 \left(\frac{r}{R_2} \right)^{-n_3-1} \right] \cos\left(n_3 \alpha \right)$$
$$- \sum_{n_3} \left[n_3 C^3 \left(\frac{r}{R_3} \right)^{n_3-1} - n_3 D^3 \left(\frac{r}{R_2} \right)^{-n_3-1} \right] \sin\left(n_3 \alpha \right), \tag{6}$$

where: B_{3r} is the radial component of air gap subdomain magnetic density, B_{3t} is the tangential component of air gap subdomain magnetic density, A^3, B^3, C^3 and D^3 are the harmonic coefficient of the air gap subdomain, n_3 is the logarithm of spatial harmonics in the air gap subdomain.

Permanent magnet subdomain magnetic density can be expressed as:

$$B_{4r} = -\frac{1}{r} \sum_{n_4} \left[C^4 \left(\frac{r}{R_2} \right)^{n_4} + D^4 \left(\frac{r}{R_1} \right)^{-n_4} \right] \sin\left(\alpha + \frac{\theta_0 R_1}{2R_2} - \alpha_i \right)$$
$$- \frac{1}{r} \frac{n_4 \pi}{b_{0a}} \sum_{n_4} \mu_0 \left(\frac{M_{rl} - M_{\alpha l}}{2} \ln r \right) \sin\left(\frac{n_4 \pi}{b_{\text{sk}}} \right) \left(\alpha + \frac{\theta_0 R_1}{2R_2} - \alpha_i \right), \tag{7}$$

$$B_{4r} = \frac{B^4}{r} - \sum_{n_4} \left[n_4 C^4 \left(\frac{r}{R_2} \right)^{n_4-1} - n_4 D^4 \left(\frac{r}{R_1} \right)^{-n_4-1} \right] \cos\left(\alpha + \frac{\theta_0 R_1}{2R_2} - \alpha_i \right)$$
$$- \sum_{n_4} \mu_0 \left(\frac{M_{rl} - M_{\alpha l}}{2r} \right) \cos\left(\frac{n_4 \pi}{b_{\text{sk}}} \right) \left(\alpha + \frac{\theta_0 R_1}{2R_2} - \alpha_i \right), \tag{8}$$

where: B_{4r} is the radial component of permanent magnet subdomain magnetic density, B_{4t} is the tangential component of permanent magnet subdomain magnetic density, A^4, B^4, C^4 and D^4 are the harmonic coefficient of the permanent magnet subdomain, n_4 is the logarithm of spatial harmonics in the permanent magnet subdomain, R_2 is the radius of the circle where the permanent magnet is located after segmented equivalence, R_1 is the radius of the circle where the rotor core is located.

By utilizing the aforementioned calculation formulas for subdomain magnetic densities, one can derive the distribution of the air gap magnetic density within the motor. The fundamental wave amplitude of the air gap magnetic density calculated through the subdomain method is 0.878 T, while the amplitude obtained via the finite element method is 0.864 T. As both values are relatively similar, the resultant air gap magnetic density value can be considered reasonable.

3. Optimization of rotor structure for hybrid magnetic circuit motor

3.1. Optimization of permanent magnet parameters for hybrid magnetic circuit motor

The output performance of a motor depends not only on the dimensions of the stator and rotor, but also on the permanent magnet's size. To minimize the permanent magnet's volume, while maintaining the output torque of the motor, optimizing the permanent magnet's placement position is crucial. The magnetic poles on each rotor pole are of equal size, and only one set of poles is used to represent the parameter information. The remaining poles are then optimized based on the same parameter size. Figure 3 provides a schematic diagram of each parameter. The optimization objectives include the peak value of air gap magnetic density, total harmonic distortion of air gap magnetic density (THD), and output torque. Table 2 displays the range and initial values for each variable.
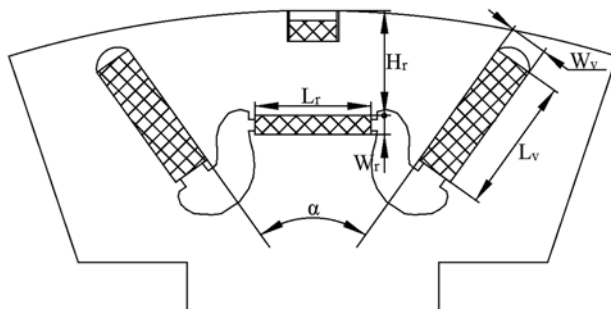
Fig. 3. Permanent magnet parameters for the hybrid magnetic circuit motor

To guarantee the rotor's strength and reduce magnetic leakage, position the arc-shaped magnetic barrier 2 mm from the outer edge of the rotor. The direct current excitation current should be set to zero, and the variables should be optimized. Firstly, retain the initial values of the remaining 5 variables and choose the optimal value for L_v based on the simulation of the shifting trends of each optimization objective. Maintain the optimal value of L_v and select W_v for optimization while keeping the remaining variables unchanged. This method yields the optimal value of Wv. The same procedure can be applied to obtain optimal values for all variables.

Table 2. The range of values for each variable

Parameter name	Value range	Initial value	Unit
The length of the V-shaped PM	$9 \leq L_v \leq 12$	10.5	mm
The width of the V-shaped PM	$3 \leq W_v \leq 4.5$	3.6	mm
The angle of the V-shaped PM	$40 \leq \alpha \leq 80$	60	°
The length of the radial PM	$6 \leq L_r \leq 10$	8	mm
The width of the radial PM	$1 \leq W_r \leq 3$	2	mm
The radial PM distance from the outer diameter of the rotor	$7.5 \leq H_r \leq 9.5$	8.5	mm

Figure 4 shows the waveform of THD and output torque with different parameters. With the continuous increase of L_v, the THD shows a fluctuating increasing trend. The output torque rapidly increases, and the torque ripple continuously decreases. As W_v continues to increase, the overall waveform of the air gap magnetic density increases, the THD shows an upward trend. After $W_v = 3.9$ mm, the increase in output torque slows down, and torque ripple gradually decreases with the increase of W_v. Along with α increases, the peak value of magnetic density decreases first and then increases, and the THD decreases. The output torque continues to increase, and the torque ripple gradually decreases. The peak value of air gap magnetic density and THD continuously increase with the increase of L_r, which will generate higher output torque. With the increase of W_r, the peak value of air gap magnetic density rapidly increases, the THD slowly increases, and higher output torque is generated, but the increase is not significant. As H_r increases, the peak value of air gap magnetic density increases linearly, and the THD first decreases and then increases, resulting in a slow increase in output torque. Table 3 shows the optimal magnetic pole parameters of the hybrid magnetic circuit motor.

Table 3. The optimal magnetic pole parameters of the hybrid magnetic circuit motor

Symbol	Value	Unit	Symbol	Value	Unit
L_v	12	mm	L_r	10	mm
W_v	3.9	mm	W_r	2	mm
α	80	°	H_r	8.5	mm

The purpose of adding surface mounted permanent magnets is to create a more sinusoidal air gap magnetic density waveform, although their impact on improving peak air gap magnetic density is restricted. As a result, it is possible to select common permanent magnets available in the market. The length of surface mounted permanent magnets in this case is 3 mm, while their width is 1 mm.

(a)

(b)

(c)

(d)

(e)

(f)
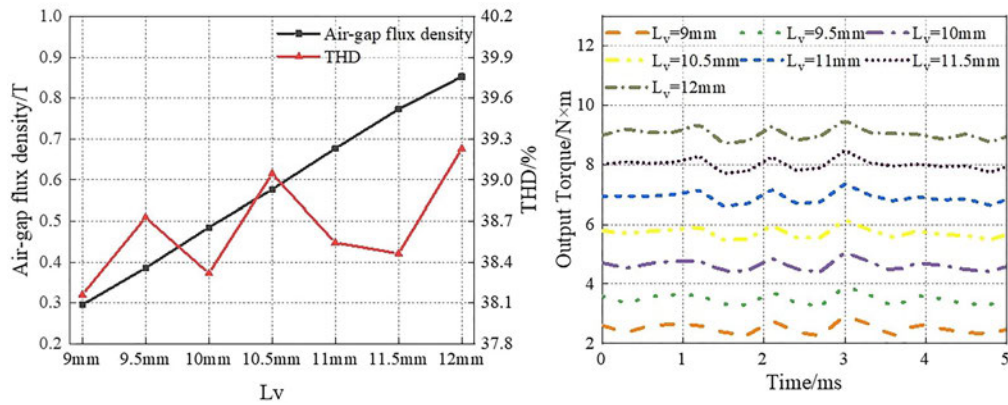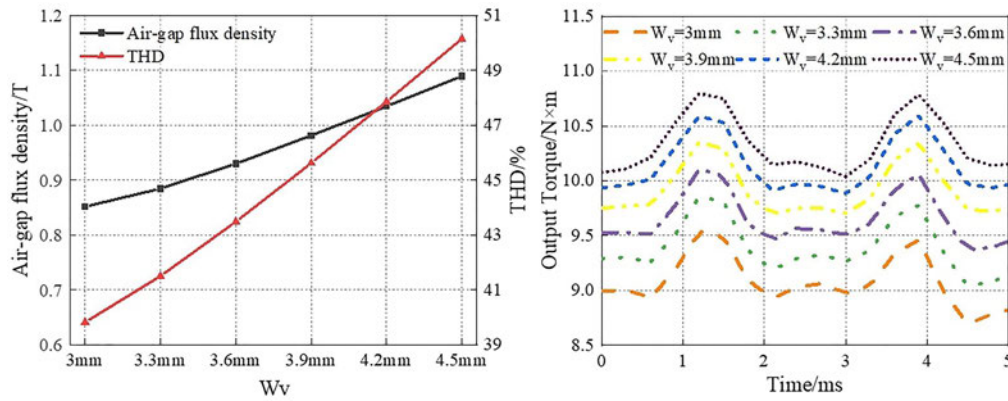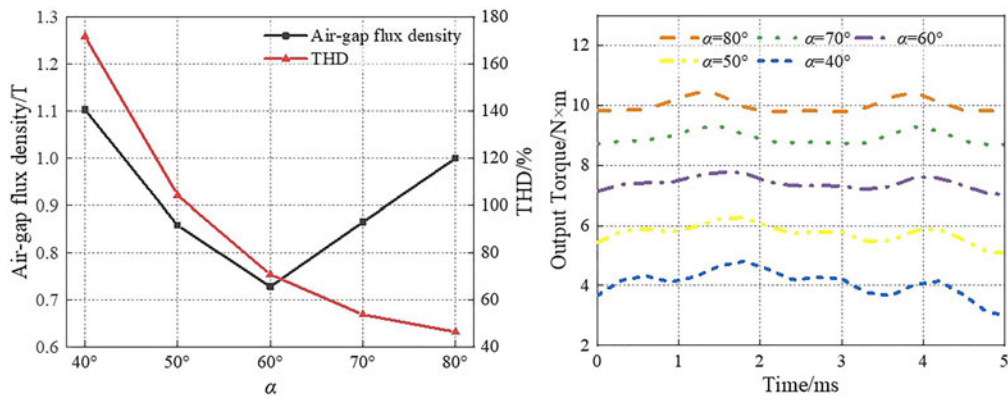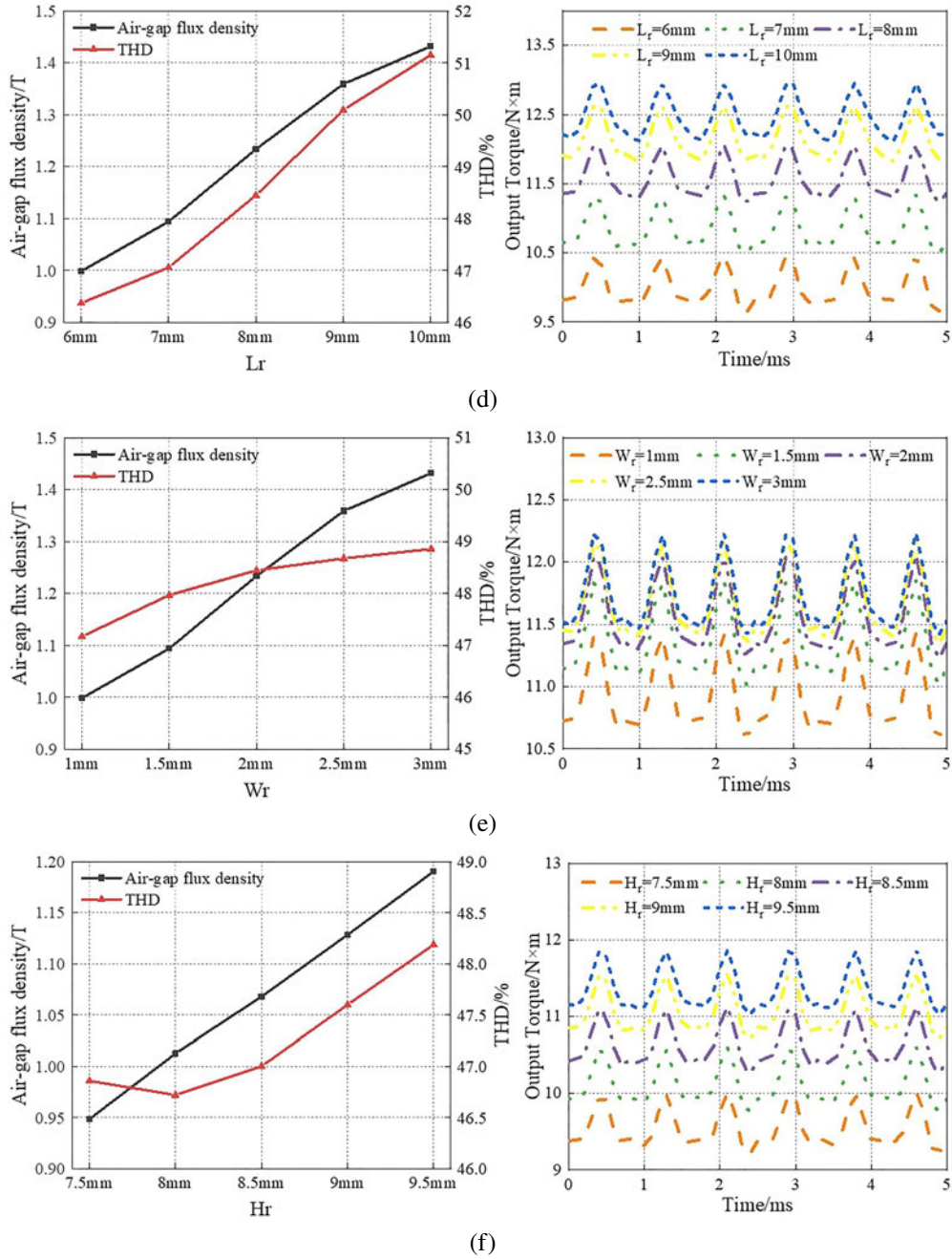
Fig. 4. Waveform variation of THD and output torque with different parameters: (a) L_v; (b) W_v; (c) α; (d) L_r; (e) W_r; (f) H_r

3.2. Improvement and optimization of the hybrid magnetic circuit motor

When a magnetic barrier is not used, magnetic leakage at the end of the magnetic pole is significant. The use of a conventional magnetic barrier in a combined magnetic pole creates the possibility of pole-to-pole leakage between the V-shaped permanent magnet and the radial permanent magnet, which eventually causes a decrease in the effective magnetic flux. This paper proposes the design of a tube-shaped magnetic barrier for salient pole rotors. The purpose of the barrier is to reduce the end leakage of permanent magnets and improve the alignment of magnetic field lines. The barrier is located between the V-shaped and radial permanent magnets. The shape and positioning of the barrier affect the air gap's magnetic density, which in turn affects the output torque. For optimal results, the barrier should be wider than 3 mm. Please refer to Fig. 5 for a schematic of the tube-shaped magnetic barrier.
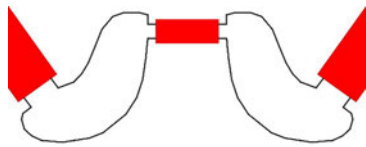
Fig. 5. Schematic diagram of tubular magnetic barrier

Figure 6 shows the direction of magnetic field lines under different magnetic barrier conditions. When the permanent magnet is embedded in the salient rotor and the magnetic pole end is not equipped with a magnetic barrier, the magnetic leakage at the ends A, B, and C is severe. When a traditional magnetic barrier is installed at the end of the magnetic pole, the magnetic leakage at the ends A, B, and C is improved, reducing some of the leakage. However, the magnetic field between the magnetic poles at D is not separated, making the magnetic field direction slightly different from the magnetic circuit analysis. When a tube type magnetic barrier is installed, its suppression effect on magnetic leakage is significant, and the direction of the magnetic field line is consistent with the direction of the magnetic circuit analysis.
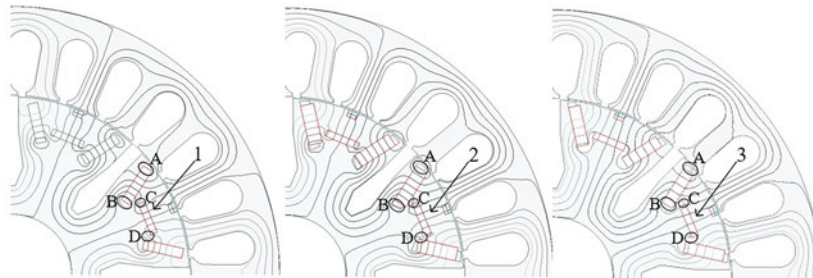
Fig. 6. Direction of magnetic field lines under different magnetic barrier conditions: 1 – no magnetic barrier; 2 – traditional magnetic barrier; 3 – tubular magnetic barrier

Figure 7 displays the air gap magnetic density under various magnetic barriers. Tubular magnetic barriers effectively enhance the peak value of air gap magnetic density. The peak values of air gap magnetic density corresponding to nonmagnetic barriers, traditional magnetic barriers, and tubular magnetic barriers are 0.78 T, 0.98 T, and 1.17 T, respectively. Compared to the scenario lacking magnetic barriers, the peak value of air gap magnetic density of tubular magnetic

barriers has increased by 50.2%. In comparison to standard magnetic barriers, the peak air gap magnetic density value has increased by 19.7%. Under three different forms of magnetic barriers, the fundamental amplitude of the tube-type magnetic barrier is higher while the harmonic content of the 3rd, 4th, and 9th harmonics is lower compared to the other two forms of magnetic barriers. The total harmonic distortion (THD) values corresponding to the non-magnetic barrier, traditional magnetic barrier, and tube-type magnetic barrier are 45.32%, 52.56%, and 45.17%, respectively. The peak air gap magnetic density of a tubular magnetic barrier is enhanced, while the distortion rate of its waveform is reduced. The utilization rate of permanent magnets is improved, and their magnetic focusing ability is increased through the design of this type of magnetic barrier.

(a)   (b)
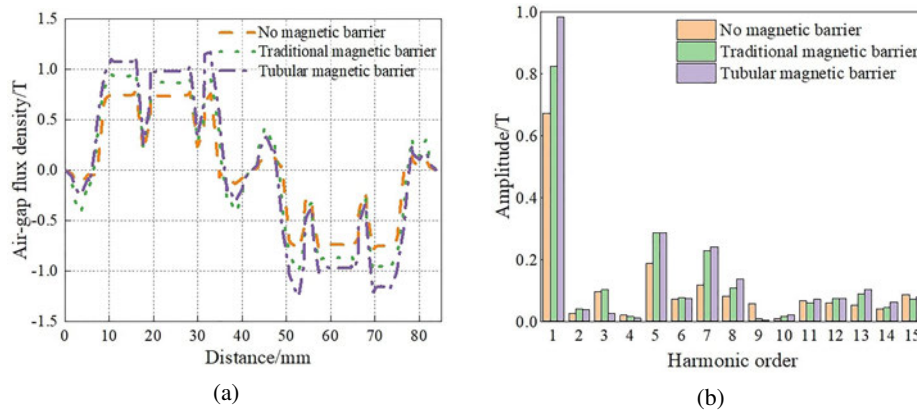
Fig. 7. The air-gap flux density of the hybrid magnetic circuit motor under different magnetic barrier conditions: (a) air gap magnetic density waveform; (b) amplitude of each harmonic

When the rotor pole surface is structured eccentrically, meaning that the center of the outer circular surface doesn't align with the axis, the distance between the center of the outer circular surface of the rotor and the axis is referred to as the rotor's eccentricity. The motor's air gap length alters and this impacts the air gap magnetic density distribution in the circumferential direction. As a result, the high-order harmonic content in the induced electromotive force decreases, weakening the cogging torque. Refer to Fig. 8 for a diagram of the rotor's eccentricity structure.
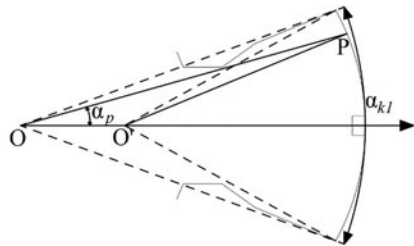
Fig. 8. The geometry of the salient pole rotor

Figure 9 illustrates the air gap magnetic density under the eccentricity of different salient rotor polar surfaces. The peak value of the air gap magnetic flux density waveform increases as the eccentricity increases. The peak value exhibits a significant increase when the eccentricity exceeds 16 mm. The fundamental wave content of the air gap magnetic density under different

polar eccentricity ranges from 0.6 T to 0.7 T. The third harmonic increases with higher eccentricity, whereas the fifth harmonic decreases. For eccentricity between 2 mm and 10 mm, air gap magnetic density's peak value gradually rises. THD initially reduces as eccentricity increases, though it later increases. Therefore, a higher air gap magnetic flux peak value and lower THD result from 16 mm eccentricity.

(a) (b)
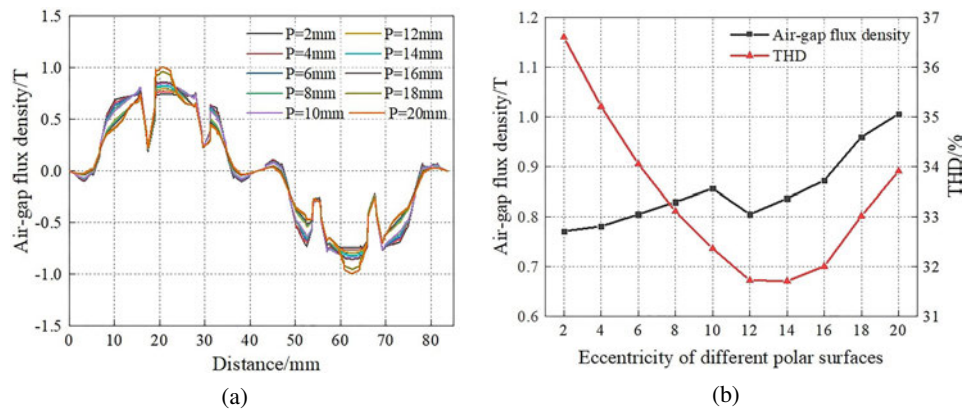
Fig. 9. The air-gap flux density of the hybrid magnetic circuit motor under different the eccentricity of different salient rotor polar surfaces: (a) air gap magnetic density waveform; (b) THD

Figure 10 shows the comparison of the air gap magnetic density before and after rotor eccentricity. The air gap magnetic density waveform before rotor eccentricity shows a rectangular wave, while the air gap magnetic density waveform after rotor eccentricity is more sinusoidal in distribution, with increased amplitude and a notable decline in high-order harmonic content. THD values prior to and after optimization are 38.18% and 27.37%, respectively, demonstrating a significant reduction in amplitude.

(a) (b)
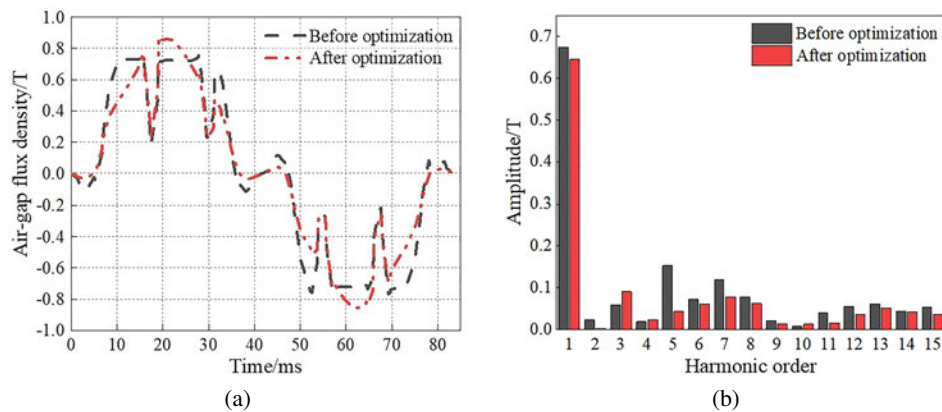
Fig. 10. Comparison of the air gap magnetic density before and after pole eccentricity: (a) air gap magnetic density waveform; (b) amplitude of each harmonic

4. Simulation analysis of electromagnetic coupling in hybrid magnetic circuit motor

Improvements have been made to the design of the hybrid magnetic circuit motor, resulting in a reasonable parameter combination being obtained. An electromagnetic coupling simulation was then performed, with Fig. 11 showing the air gap magnetic density of the motor. The waveform of the air gap magnetic density is more sinusoidal, displaying a fundamental amplitude of 0.884 T. The high harmonic content of the air gap magnetic density is less than 0.2 T, leading to a THD of 29.57%.
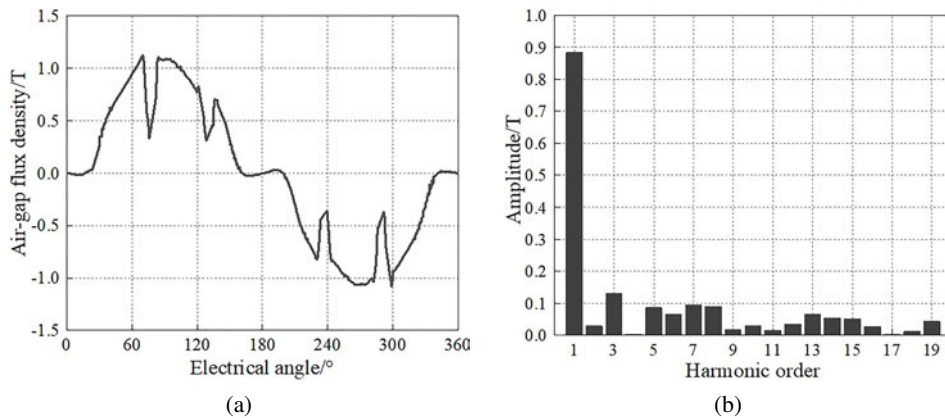
Fig. 11. The air-gap flux density of the hybrid magnetic circuit motor: (a) air gap magnetic density waveform; (b) amplitude of each harmonic

Figure 12 displays the diagrams for magnetic density cloud, magnetic flux vector, and magnetic flux line direction in a hybrid magnetic circuit motor. The magnetic field between the V-shaped permanent magnet and the radial permanent magnet is parallel, thus preventing irreversible demagnetization. The distribution of magnetic flux lines is even, and the addition of radial and surface-mounted permanent magnets enhances the magnetic field effect, leading to an increased utilization of the magnetic poles and improved output performance of the motor. The permanent magnet portion of the hybrid magnetic circuit motor exhibits a periodic and uniform circumferential distribution of the magnetic field. The presence of magnetic barriers near the outer circle of the rotor leads to a magnetic density of 2.2 T in the V-shaped permanent magnet. At this level, the magnetic density becomes saturated, which reduces the leakage magnetic flux, allowing the magnetic field lines of the magnetic poles to pass through the air gap more effectively, creating effective magnetic flux.

Figure 13 displays the magnetic density cloud diagram of the hybrid magnetic circuit motor under different excitation currents. When the excitation current is at 3 A, the generated excitation magnetic field is strong, and the magnetic density at the connection between the pole body and the pole shoe can reach 2 T. The magnetic density in the salient pole rotor area reaches saturation. When the excitation current is 2 A, the magnetic density in the salient rotor area is slightly lower than that at 3 A. Nevertheless, this can still produce a robust magnetic density. When the excitation current is positive, the hybrid magnetic circuit motor can provide significant output torque with
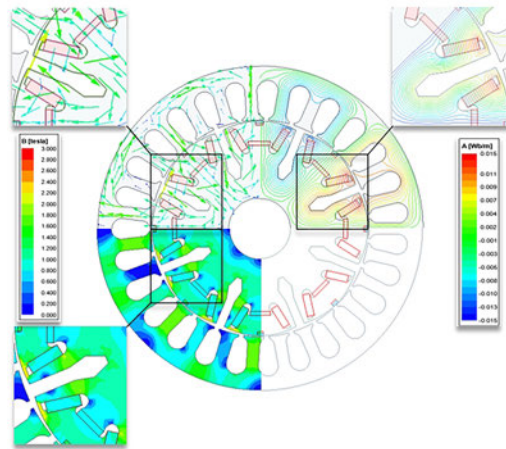
Fig. 12. The static magnetic field distribution of the hybrid magnetic circuit motor

(a) 3A

(b) 2A

(c) -2A

(d) -3A
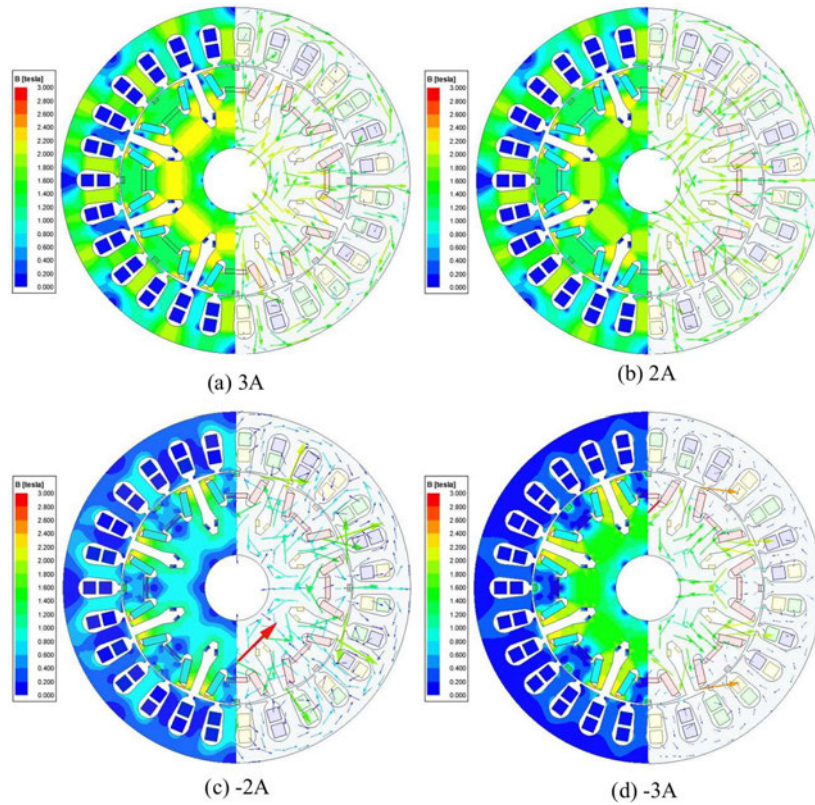
Fig. 13. Flux density cloud of a hybrid magnetic circuit motor under different excitation currents

strong magnetic density. In contrast, when the excitation current is –2 A, the magnetic density decreases in the stator core. Furthermore, the magnetic density in the stator yoke is nearly 0 T. When the excitation current reaches –3 A, the magnetic density within the stator core is further reduced, causing the magnetic density throughout the stator to approach 0 T. When the excitation current is below 0, the electric excitation magnetic field weakens the permanent magnet magnetic field. This results in weaker magnetic density within the hybrid magnetic circuit motor, providing a lower output torque.

Figure 14 depicts the hybrid magnetic circuit motor's output torque at the rated load. The average output torque at rated state is approximately 15.5 N·m, which is close to the design value. Additionally, the torque ripple stands at only 3.23%. This motor delivers steady output torque and satisfies the specifications for vehicle use under the rated state. Figure 15 shows the relationship between the output torque and the excitation current. When the excitation current falls below 0, it significantly weakens the magnetic field. The output torque only reaches 1.5 N·m at –3 A, pointing towards a noteworthy potential for the magnetic field to expand. When the excitation current becomes positive, the output torque increases from 12.21 N·m to 16.87 N·m with an increase in the excitation current. At this point, the motor can play a role in deceleration and torque amplification.
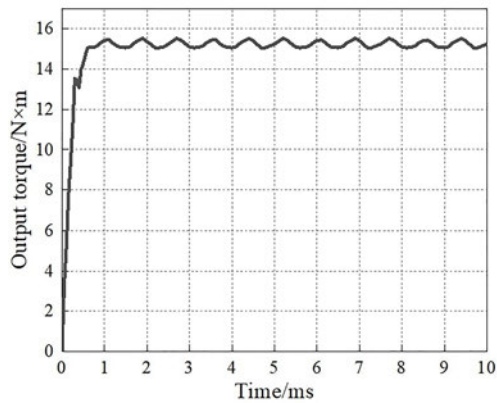
Fig. 14. Rated output torque of the hybrid magnetic circuit motor
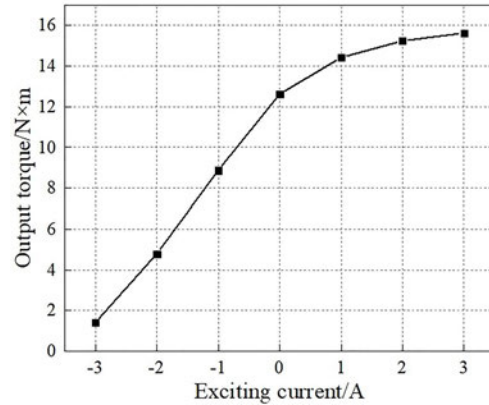
Fig. 15. The relationship between output torque and excitation current

5. Experimental confirmation

Both the theory and finite element analysis confirm the excellent magnetic gathering ability and high efficiency of the hybrid magnetic circuit motor, which features controllable output torque. Its output capacity has been further tested through experiments. The prototype of the hybrid magnetic circuit motor is depicted in Fig. 16. Figure 17 presents a testing platform, specially designed to assess the performance of the prototype.

Figure 18 shows the rated voltage output characteristic curve of the prototype. The prototype is capable of stable torque generation under the nominal voltage characteristics. When the speed reaches the rated speed, the prototype power is about 5 kW, and the efficiency can reach 92.3%,

which meets the design requirements. Figure 19 shows the peak power output characteristic curve of the prototype. When the motor is overloaded, its efficiency decreases due to an increase in copper loss.
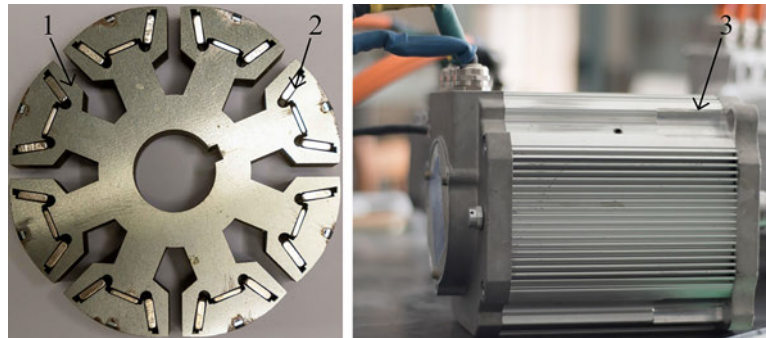
Fig. 16. Prototype: 1 – rotor core; 2 – permanent magnets; 3 – overall unit
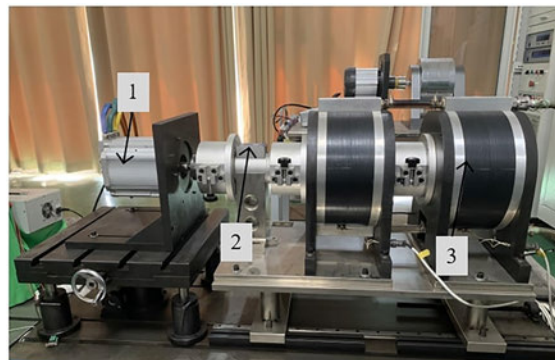
Fig. 17. Experimental platform: 1 – prototype; 2 – torque and speed sensor; 3 – electric dynamometer
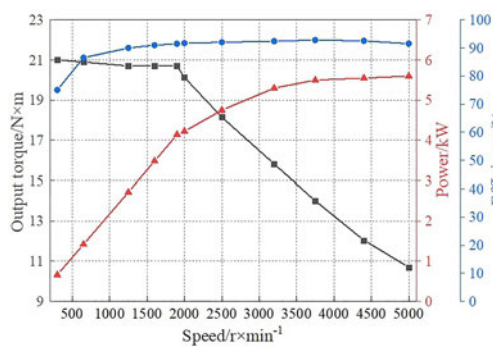
Fig. 18. Rated voltage output characteristic of prototype
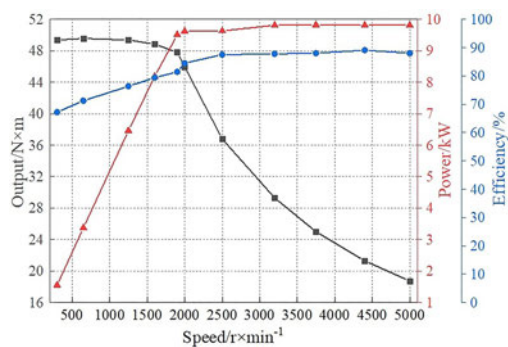
Fig. 19. Peak power output characteristic of prototype

Figure 20 illustrates the variation curve of the output torque with the excitation current at rated speed. At 2 A of excitation current, the output torque is approximately 16 N·m. Additionally, the motor possesses a particular magnetization capability. The experimental outcomes align with the simulation data and indicate that the hybrid magnetic circuit motor design performs well. This design meets the complex and variable operating conditions required of vehicles.
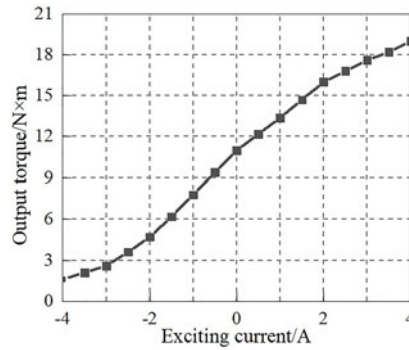
Fig. 20. Magnetization characteristic of prototype

6. Conclusions

This article optimizes the design of a hybrid magnetic circuit motor with salient pole electromagnetic and permanent magnets combination. In addition, this paper also draws the following conclusions:

1. The magnetic field of the permanent magnet portion of the non-uniform magnetic potential source is analyzed using the subsection equivalent method. The magnetic pole parameters have a substantial influence on the magnetic field distribution. To obtain the optimal parameters for each magnetic pole, the control variates are utilized to optimize the combined magnetic poles. A tubular magnetic barrier with outstanding magnetic isolation performance is created. Compared to the conventional magnetic barrier, the amplitude of the fundamental wave of the magnetic field across the air gap has increased by 19.7%. This alteration has led to an improvement in the distribution of the sinusoidal wave across the air gap's magnetic density. This has contributed to an improvement in the permanent magnet's efficiency. The optimization of the rotor eccentricity has resulted in a reduction in the THD from 38.18% to 27.37%. Additionally, the pole eccentricity has facilitated a transformation of the magnetic density waveform from a rectangular wave to a sinusoidal wave;

2. Carrying out an electromagnetic coupling simulation analysis on a hybrid magnetic circuit motor, it was determined that the optimal amplitude of the air gap magnetic density fundamental wave is 0.884 T with a THD of 29.57%. Additionally, the rotor magnetic density distribution is uniform and the magnetic flux vector is reasonable. The synthesized magnetic field level can be stably adjusted under different excitation currents, resulting in stable output torque. After carrying out tests and analyzing the prototype, we discovered that the enhanced motor delivers strong output performance and proves to be adaptable to challenging and ever-changing operating conditions.

References

[1] Guo Z.H., Sun S.J., Wang Y.S., *Impact of New Energy Vehicle Development on China's Crude Oil Imports: An Empirical Analysis*, World Electric Vehicle Journal, vol. 14, no. 2, pp. 46–49 (2023), DOI: 10.3390/wevj14020046.

[2] Benites-Lazaro L.L., Giatti L., Giarolla A., *Topic Modeling Method for Analyzing Social Actor Discourses on Climate Change, Energy and Food Security*, Energy Research & Social Science, vol. 45, pp. 318–330 (2018), DOI: 10.1016/j.erss.2018.07.031.

[3] Chen S., Wei Z.N., Gu W., Guo Q.L., *Transformation and Transformation of Energy Systems under the Goal of Carbon Neutrality: Multi Energy Flow Synergy Technology*, Electric Power Automation Equipment, vol. 41, no. 9, pp. 3–12 (2021), DOI: 10.16081/j.epae.202109037.

[4] Wrobel R., *Thermal Management of Electrical Machines for Propulsion – Challenges and Future Trends*, Archives of Electrical Engineering, vol. 71, no. 1, pp. 175–187 (2022), DOI: 10.24425/aee.2022.140204.

[5] Zhang S.X., Ma B.Y., *Development Trend of World Energy and Future Development Directions of China's Energy*, Natural Resource Economics of China, vol. 32, no. 10, pp. 20–27 (2019), DOI: 10.19676/j.cnki.1672-6995.0000285.

[6] Cao S.S., *Research on the Development Strategy and Countermeasures of New Energy Vehicles based on Core Competitiveness*, Modern Management Forum, vol. 6, no. 12, pp. 129–138 (2022), DOI: 10.18686/MODERN-MANAGEMENT-FORUM.V6I12.6946.

[7] Yang C.X., Wang K., Liu Z.Y., *Research on Magnetic Regulation Characteristics of Axial-radial Flux Type Permanent Magnet Synchronous Machine*, Archives of Electrical Engineering, vol. 71, no. 1, pp. 75–90 (2022), DOI: 10.24425/aee.2022.140198.

[8] Paplicki P., *A Novel Rotor Design for a Hybrid Excited Synchronous Machine*, Archives of Electrical Engineering, vol. 66, no. 1, pp. 29–40 (2017), DOI: 10.1515/aee-2017-0003.

[9] Lin N., Wang D., Wei K., *Mathematical Model and Equivalent Analysis of a Novel Hybrid Excitation Synchronous Machine*, Transactions of China Electrotechnical Society, vol. 32, no. 3, pp. 149–156 (2017), DOI: 10.19595/j.cnki.1000-6753.tces.2017.03.017.

[10] Chai W.P., Kwon J., Kwon B., *Analytical Design of a Hybrid-Excited Wound Field Synchronous Machine for the Improvement of Torque Characteristics*, IEEE Access, vol. 8, pp. 87414–87421 (2020), DOI: 10.1109/ACCESS.2020.2993317.

[11] Wardach M., Paplicki P., Palka R., *A Hybrid Excited Machine with Flux Barriers and Magnetic Bridges*, Energies, vol. 11, no. 3, pp. 676–687 (2018), DOI: 10.3390/en11030676.

[12] Matsui N., *Design and Control of Variable Field Permanent Magnet Motors*, IEEJ Transactions on Electrical and Electronic Engineering, vol. 14, no. 7, pp. 966–981 (2019), DOI: 10.1002/tee.22891.

[13] Shirzad E., Rahideh A., *Analytical Model for Brushless Double Mechanical Port Flux-Switching Permanent Magnet Machines*, IEEE Transactions on Magnetics, vol. 57, no. 10, pp. 1–13 (2021), DOI: 10.1109/TMAG.2021.3104938.

[14] An Y.S., Ma C.G., Li X., *Analytical Modeling of Air-gap Magnetic Field and Multi-objective Optimization Interior Permanent Magnet Synchronous Motor for Electric Vehicles*, China Journal of Highway and Transport, vol. 36, no. 1, pp. 253–262 (2023), DOI: 10.19721/j.cnki.1001-7372.2023.01.020.

[15] Ladghem Chikouche B., Ibtiouen R., *Analytical approach for spoke-type permanent magnet machine including finite permeability of iron core*, COMPEL – The International Journal for Computation and Mathematics in Electrical and Electronic Engineering, vol. 39, no. 2, pp. 333–352 (2020), DOI: 10.1108/COMPEL-04-2019-0143.

[16] Gysen B.L.J., Meessen K.J., Paulides J.J.H., *General Formulation of the Electromagnetic Field Distribution in Machines and Devices Using Fourier Analysis*, IEEE Transactions on Magnetics, vol. 46, no. 1, pp. 39–52 (2010), DOI: 10.1109/TMAG.2009.2027598.

[17] Zhu Z.Q., Wu L.J., Xia Z.P., *An Accurate Subdomain Model for Magnetic Field Computation in Slotted Surface-Mounted Permanent-Magnet Machines*, IEEE Transactions on Magnetics, vol. 46, no. 4, pp. 1100–1115 (2010), DOI: 10.1109/TMAG.2009.2038153.